

Comparative Molecular Dynamics Study of the Roles of Anion–Cation and Cation–Cation Correlation in Cation Diffusion in $\text{Li}_2\text{B}_{12}\text{H}_{12}$ and $\text{LiCB}_{11}\text{H}_{12}$

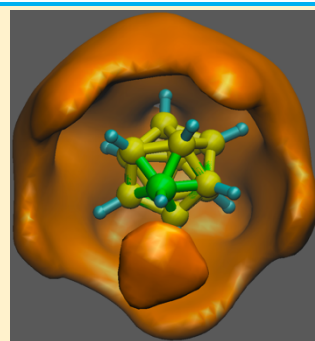
Kartik Sau,^{1,*} Tamio Ikeshoji,¹ Sangryun Kim,² Shigeyuki Takagi,² and Shin-ichi Orimo^{2,3}

¹Mathematics for Advanced Materials Open Innovation Laboratory (MathAM–OIL), National Institute of Advanced Industrial Science and Technology (AIST), c/o Advanced Institute of Material Research (AIMR), Tohoku University, Sendai 980–8577, Japan

²Institute for Materials Research (IMR), Tohoku University, Sendai 980–8577, Japan

³Advanced Institute for Materials Research (AIMR), Tohoku University, Sendai 980–8577, Japan

ABSTRACT: Complex hydrides are potential candidates for the solid electrolyte of all-solid-state batteries owing to their high ionic conductivities, in which icosahedral anion reorientational motion plays an essential role in high cation diffusion. Herein, we report molecular dynamics (MD) simulations based on a refined force field and first-principles calculations of the two complex hydride systems $\text{Li}_2\text{B}_{12}\text{H}_{12}$ and $\text{LiCB}_{11}\text{H}_{12}$ to investigate their structures, order–disorder phase-transition behavior, anion reorientational motion, and cation conductivities. For both systems, force-field-based MD successfully reproduced the structural and dynamical behavior reported in experiments. Remarkably, it showed an entropy-driven order–disorder phase transition associated with high anion reorientational motion. Furthermore, we obtained comparative insights into the cation around the anion, cation site occupancy in the interstitial space provided by anions, cation diffusion route, role of cation vacancies, anion reorientation, and effect of cation–cation correlation on cation diffusion. We also determined the factors that activate anion reorientational motion leading to a low to high conductivity phase transition. These findings are of fundamental importance in fast ion-conducting solids to diminish the transition temperature for practical applications.



1. INTRODUCTION

There is ever-increasing demand for high energy density electrochemical storage systems imposing a question mark on present battery technology, which cannot satisfactorily meet all of the requirements for powering portable devices, automobiles, and electric grids.^{1–5} All-solid-state batteries (ASSBs) are promising to overcome the existing limitations of present Li-ion batteries, which suffer from flammability, limited energy density, and stability issues. Recently, significant progress has been made in development of ASSBs,⁶ where high ionic conductivity is one of the inevitable prerequisites for the electrode and electrolyte. The electrolytes in ASSBs are largely based on Li^+ ion-conducting materials,^{7–16} such as $\text{Li}_{10}\text{GeP}_2\text{S}_{12}$ (LISICON-like),⁸ $\text{Li}_6\text{PS}_5\text{Br}$ (argyrodite),^{17,18} LiBH_4 ,¹⁹ $\text{Li}_2\text{B}_{12}\text{H}_{12}$,²⁰ $\text{Li}_{6.55}\text{La}_3\text{Zr}_2\text{Ga}_{0.15}\text{O}_{12}$ (garnet),^{21,22} $\text{Li}_{1.2}\text{Al}_{0.2}\text{Ti}_{1.8}(\text{PO}_4)_3$ (NASICON-type),²³ and $\text{Li}_{0.34}\text{La}_{0.51}\text{TiO}_{2.4}$ (perovskites),^{24,25} in which the ionic conductivity is comparable with those of present days liquid electrolytes. However, the current state of the art is not at the level to meet all of the challenges of ASSBs.

Complex borohydrides are considered to be outstanding candidates for the solid electrolyte of ASSBs because of their excellent Li- or Na-ion conductivity (exceeding $10^{-1} \text{ S cm}^{-1}$).^{4,26–}

³⁴ In addition, this enables a wide range of chemical substitutions

to open up the possibility of discovering even better ion-conductive materials. This series of materials shows a unique ion transport feature, where cation motion and anion reorientational motion coexist. This type of behavior is also observed in other promising class materials (e.g., Na_3PS_4).^{38–40} The anion size is larger in complex closo-borohydrides than in Na_3PS_4 , which facilitates a relatively wide corridor for the Li^+ ion, resulting in a vacancy-rich structure. However, most of the materials exhibit high ionic conductivity at high temperature, and the room temperature conductivity is low.

In the last few years, enormous effort has been dedicated to maximizing the room temperature ionic conductivity. For instance, a larger cation size can reduce the transition temperature.^{42,43} Recently, remarkable reduction in the transition temperature has been reported in C-substituted closo-boranes.⁴⁴ In particular, alloying of two different C-substituted closo-boranes could decrease the transition temperature to close to room temperature.³² Therefore, understanding the factors that enable anion reorientation, resulting in reduction of transition temperature, would be an essential guideline to synthesize a fast ion-conducting material. In all of the high conductivity phases in this series, anion reorientation is a common key feature that also makes challenging to find high temperature structural details from experiments because of high anionic reorientation. Recently, a few

first-principles MD (FPMD) studies have been reported.^{45–47} However, they were mostly at high temperature and limited to a few tens of picoseconds, in which anions hardly show complete reorientational motion. Additionally, capturing the phase transition behavior from FPMD is almost impossible. The above gap can be fulfilled using force-field based molecular dynamics (MD) simulation that can provide such valuable atomic-level detail. In particular, it can accurately capture anion reorientational motion and phase transition behavior.

Herein, we report a thorough comparative MD study of the $\text{Li}_2\text{B}_{12}\text{H}_{12}$ (LBH) and $\text{LiCB}_{11}\text{H}_{12}$ (LCBH) solid electrolyte materials to understand the entropy-driven phase transition behavior, role of cation–cation correlation, anion reorientation, and cation diffusion.^{48,49} Finally, we determined the factors that activate the anion reorientational motion, resulting in low transition temperature. We used reported interatomic potential parameters for LBH, and refined the parameters for the similar structure of the LCBH system. The potential models satisfactorily reproduced the structure, and phase transition behavior (Section 3.1). Comparison of lithium-ion diffusion and its atomistic distribution for two different phases is reported in Sections 3.2 and 3.3, respectively. Coupling of anions reorientational motion and cation diffusion, cation-cation correlation are reported in Section 3.4, and 3.5, respectively. Finally, we discuss about the influencing factors responsible for diminishing the transition temperature (Sections 3.2).

2. METHODOLOGY

2.1 Interatomic Potential. To perform MD simulations of LBH and LCBH, we used a combination of Buckingham, harmonic bond, and angle-type potentials:

$$U(r, \theta) = U_{\text{Coulomb+Buckingham}}(r) + U_{\text{bond}}(r) + U_{\text{angle}}(\theta) \quad (1)$$

$$U_{\text{Coulomb+Buckingham}}(r) = \frac{q_i q_j}{4\pi\epsilon_0 r} + A \exp\left(-\frac{r}{\rho}\right) - \frac{C}{r^6},$$

$$U_{\text{bond}}(r) = \frac{1}{2} k_r (r - r_0)^2,$$

$$U_{\text{angle}}(r) = \frac{1}{2} k_\theta (\theta - \theta_0)^2,$$

where q_i is the charge of the i th ion, A and C are the overlap repulsive energy and dispersion energy of atom pairs, respectively, and ρ determines the depth of the potential. r_0 is the equilibrium

bond distance with bond spring constant k_r , and k_θ is the angular spring constant with equilibrium angle θ_0 . The interatomic potential in eq 1 and the potential parameters were taken from our previous work.¹² A few pairs of atoms that were not available because of incorporation of C were suitably modified for the LCBH system by empirical fitting to the reported low-temperature (LT) crystallographic structure following the method reported by Kumar and Yashonath⁵⁰ and compared with the power spectrum calculated by density functional theory (DFT):

1. The short-range interaction parameters (A , ρ and C) were adjusted to reproduce the bond lengths and coordination numbers of the bonded species from X-ray diffraction.
2. The charge parameter q was tuned to reproduce the high temperature (HT) conductivity, and the spring constants were adjusted to match the vibrational frequencies.

We performed iterative MD simulations at both LT and HT until the desired accuracy was achieved. The parameters used in the present simulations for the LCBH system are listed in Table 1, and we used the previously reported parameters for the LBH system.¹²

2.2 Computational Details. Isotropic (NPT)-MD simulations were performed for the LBH and LCBH systems under the thermodynamic conditions $250 \leq T \leq 500$ K with an interval of $\delta T = 25$ or 50 K using the software package LAMMPS.⁵¹ We started the MD simulation with the crystallographically reported LT structure,⁴⁴ and the temperature was systematically increased. The temperature and pressure were allowed to fluctuate around specific values using the Nosé–Hoover thermostat and barostat.⁵² We also performed isothermal (NVT)-MD simulations at constant volume using the average lattice parameters obtained from NPT-MD at 500 K. For both LBH and LCBH systems, the simulated supercell comprised $4 \times 4 \times 4$ unit cells consisting of ~ 6000 atoms. Periodic boundary conditions were applied along all of the Cartesian directions, and the Ewald summation technique was used for the convergence of the long-range Coulombic interactions. The structural and dynamical properties were calculated for a 2 ns trajectory after a few nanoseconds for proper equilibration of the system. The velocity form of the Verlet algorithm with an integration time step $\Delta t = 0.5$ fs was used, which showed excellent energy conservation. The positions and velocities of the atoms were stored every 0.5 ps, or more

Table 1. Inter ionic potential pair parameters employed in the present study.

X	q_X (e)	A_{XLi} (eV)	A_{Xb} (eV)	A_{XH} (eV)	ρ_{XLi} (Å)	ρ_{Xb} (Å)	ρ_{XH} (Å)
Li	0.750	0.00	123.098	733.698	0.4000	0.2853	0.1953
C	0.750	123.098	0.0	0.0	0.2853	0.0	0.2853
B	0.000	123.098	0.0	0.0	0.2853	0.0	0.2853
H	−0.125	733.698	0.0	1297.251	0.1953	0.2853	0.21855

$k_{\text{B-B}} = 5.375 \text{ Å}^{-2} \text{eV}$, $r_{\text{BB0}} = 1.76 \text{ Å}$ (equilibrium bond length), $k_{\text{C-B}} = 5.375 \text{ Å}^{-2} \text{eV}$, $r_{\text{CB0}} = 1.76 \text{ Å}$ (equilibrium bond length), $k_{\text{B-H}} = 9.89 \text{ Å}^{-2} \text{eV}$, $r_{\text{BH0}} = 1.2 \text{ Å}$ (equilibrium bond length), $k_{\text{C-H}} = 150.5 \text{ Å}^{-2} \text{eV}$, $r_{\text{CH0}} = 1.09 \text{ Å}$ (equilibrium bond length), $k_{\text{B-B-H}} = k_{\text{B-C-H}} = k_{\text{C-B-H}} = 0.86 \text{ radian}^{-2} \text{eV}$, $\theta_0 = 2.077 \text{ radian}$ (equilibrium angle), $C_{\text{H-H}} = 4.3086 \text{ Å}^6 \text{eV}$.

frequently if needed. A cutoff distance of 12 Å was used for the short- and long-range interactions.

We also performed FPMD simulations of the LCBH system with the DFT Vienna Ab initio Simulation Package^{53,54} with plane-wave basis sets and projector-augmented-wave pseudopotentials^{55,56} under periodic boundary conditions to calculate the vibrational spectra and radial distribution functions (RDFs) for comparison with the forcefield-based MD results. We incorporated van der Waals density functional correlation functionals^{57,58} with the optPBE exchange functional to consider the van der Waals interactions.⁵⁹ An energy cutoff of 320 eV and $1 \times 1 \times 1$ k-point sampling were used. The simulated supercell contained $2 \times 2 \times 2$ unit cells consisting of 800 atoms for the LT structure, and the simulations were performed at 500 K for 3 ps (1 ps equilibration and 2 ps sampling) with a time step of 0.4 fs.

The self-part of van Hove correlation function, $G_s(r, t')$, is defined as the probability of finding a particle at position r after time t' averaging over N particles,⁶⁰ while the distinct part, $G_d(r, t')$, describes the behavior of two different types of particles with numbers N_1 and N_2 :⁶⁰

$$G_s(r, t') = \frac{1}{N} \langle \sum_{i=1}^N \delta(\vec{r} - (\vec{r}_i(t' + t) - \vec{r}_i(t))) \rangle, \quad (3)$$

$$G_d(r, t') = \frac{1}{N_1 N_2} \langle \sum_{j=1}^{N_1} \sum_{i=1}^{N_2} \delta(\vec{r} - (\vec{r}_i(t' + t) - \vec{r}_j(t))) \rangle.$$

The mean squared displacement (MSD) of the constituting atoms was calculated by the following equation:

$$\text{MSD} = \langle \sum_{j=1}^N [\vec{r}_j(t + t') - \vec{r}_j(t)]^2 \rangle, \quad (4)$$

where N is the number of mobile atoms in the system, $\vec{r}_j(t + t')$ is the position vector of the j th atom after time t' , and the angular brackets indicate averaging over various time origins t . The diffusion coefficient (D) was estimated from the MSD by the following equation: $D = \frac{1}{6t'} \lim_{t' \rightarrow \infty} \text{MSD}$. The ionic conductivity of the mobile cation (σ) was calculated by the Nernst–Einstein equation:

$$\sigma = \frac{nq^2 D}{H_r k_B T} \quad (5)$$

where n is the Li^+ ion density, q is the formal charge of the Li^+ ion ($+1|e|$), k_B is the Boltzmann constant, T is the temperature in Kelvin, and H_r is the Haven ratio (assumed to be unity).¹⁶

Table 2. Comparison of cell parameters calculated from NPT-MD simulation (300 K) and X-ray diffraction results.⁴⁴

Cell parameters		a (Å)	b (Å)	c (Å)	Δ (%)
LCBH	Experiment	9.67	9.49	9.73	0.6
	MD	9.73	9.55	9.79	
$\Delta = (\text{MD} - \text{Experiment}) / \text{Experiment}$					

3. RESULTS AND DISCUSSION

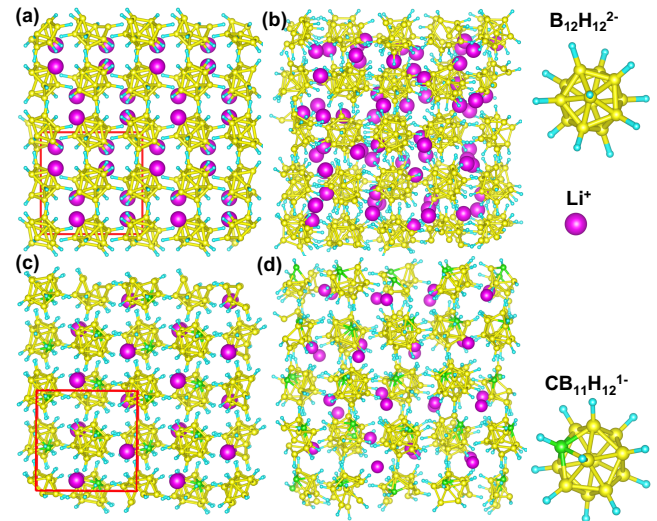


Figure 1. LT (ordered) and HT (disordered) phases of bulk $\text{Li}_2\text{B}_{12}\text{H}_{12}$ and $\text{LiCB}_{11}\text{H}_{12}$ for $2 \times 2 \times 2$ supercells. (a) LT phase of the LBH system with cubic symmetry and space group $Pa\bar{3}$. (b) HT phase of the LBH system, where cubic symmetry is preserved. However, the Li^+ ions are highly mobile and the $(\text{BH})_{12}^{2-}$ icosahedra show reorientational disorder. (c) LT phase of the LCBH system with orthorhombic symmetry. (d) HT phase of the LCBH system, where the Li^+ ions are highly mobile and the $\text{CB}_{11}\text{H}_{12}^-$ icosahedra show reorientational disorder. Li, B, C, and H ions are colored magenta, yellow, green, and cyan, respectively. The unit cells are indicated by red boxes.

3.1. Structural Details and Phase Transition. Both the LBH and LCBH structures exhibited a low to high conductivity and order to disorder transition. The LT LBH structure is referred to as the ordered α -phase, where $(\text{BH})_{12}^{2-}$ anions are occupied in face-centered cubic sites and it has $Pa\bar{3}$ symmetry. The Li^+ ions occupy near-trigonal-planar sites consisting of three $(\text{BH})_{12}^{2-}$ anions, whereas the center of the icosahedral anion is the center of an octahedral cage formed by near-trigonal-planar Li sites. This structure shows symmetry, preserving an isostructural order to disorder transition at HT (~ 650 K⁶¹ and simulated transition temperature ~ 500 K⁶²) as shown in Figure 1(a) and (b). Conversely, the LCBH system shows an orthorhombic ordered structure at LT. The anions are located at similar positions (face centers) to the LBH system, where C occupies a particular ordered vertex position in the icosahedral anion. It also shows an ordered orthorhombic to disordered cubic transition at high temperature (~ 390 K⁴²), as shown in Figure 1(c) and (d). However, experimentally, the HT structural details have not been reported.²⁹ We performed a thorough MD study to understand the phase transition and under-lying atomistic mechanism of Li^+ ion diffusion in both systems.

To validate the interatomic potential model for the LCBH system, the radial distribution functions (RDFs) calculated from MD simulation and the X-ray structure were compared (Figure S1, Supporting Information). The RDFs peaks are consistent with the FPMD peaks as well as reported experimental structure. The vibrational density of states (VDOS) was also calculated from the Fourier transform of the velocity autocorrelation function, and the VDOS was compared with FPMD and the available experimental results (Figure S2). The potential model satisfactorily reproduced the RDFs and VDOS, indicating the suitability of the potential model. We do not show the VDOS and RDF comparison for the LBH system because it has already been reported.¹²

To understand the structural transition, the volume per formula unit was calculated by averaging over a few thousand frames of the NPT-MD simulation. The calculated cell parameters showed 0.6% deviation from the reported experimental lattice parameters²⁹ at room temperature (Table 2). The cell volume variation with temperature for both the LBH and LCBH systems is shown in Figure 2. The cell volume increased with increasing temperature, and a sudden jump in the volume was observed after 325 K for the LCBH system, whereas a higher transition temperature (around 475 K) was observed for the LBH system. The sharp volume change indicates a first-order order–disorder phase transition, as has been experimentally observed for both systems.^{44,61} Remarkably, there was an almost 9% volume change in the MD simulation for the LCBH system associated with the LT to HT phase transition, which is in excellent agreement with experimental results (10% volume change).²⁹ Such a large volume change with a phase transition provides a large corridor within the anions for Li^+ ion diffusion, and the LCBH system is expected to have higher conductivity than the LBH system, which exhibited a

smaller volume change (4.6%) with the phase transition. Therefore, we can conclude that the present interatomic potential model accurately captures the structure and order of the order–disorder phase transition. The structural transition is usually difficult to achieve by FPMD and it is also challenging to achieve by forcefield-based MD.

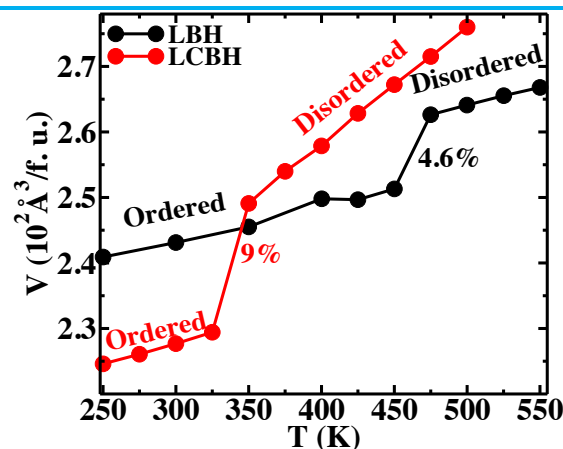


Figure 2. Volume per formula unit (f.u.) (V) as a function of temperature (T) for the LCBH system (250–500 K) and LBH system (250–550 K). Both systems exhibited a large sharp volume change (4.6% for LBH and 9% for LCBH) near the order–disorder transition temperature.

3.2. Li^+ Ion Diffusion. The MSD of the Li^+ ions (Figure 3(a) and 3(b)) and framework anions (insert of Figure 3(b)) was calculated for the LCBH system in the temperature range 250–500 K to understand cation transport and to investigate the framework stability. The MSD of the Li^+ ions in the LCBH system was fairly higher than that in the LBH system (Figure 3(b)). In contrast, the framework ions (B and H) showed relatively low MSD for both systems before the transition temperatures (inset of Figure 3(b), only the MSD of B is shown). Above the transition temperature,

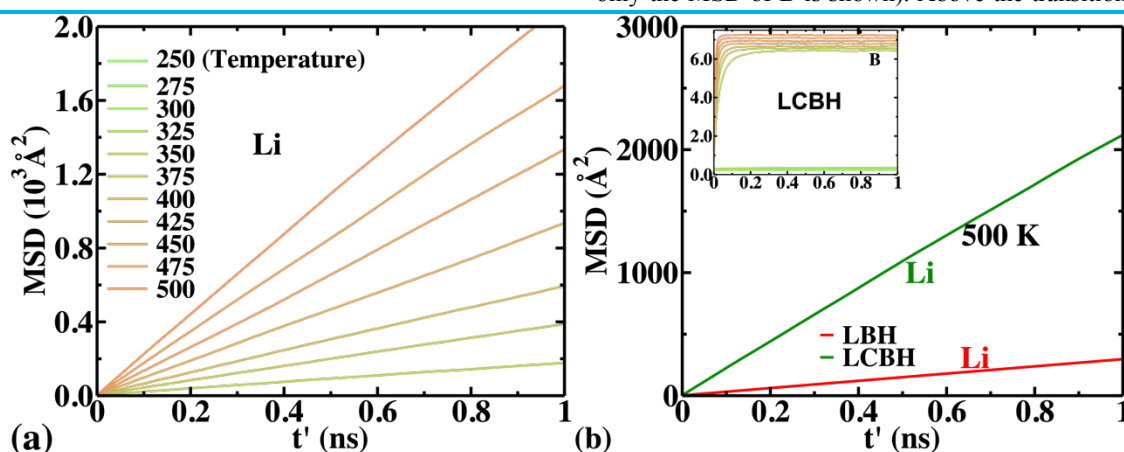


Figure 3. MSD of the LBH and LCBH systems. (a) MSD of the Li^+ ions in the LCBH system for the temperature range 250–500 K with an interval of 25 K from NPT-MD simulation (below 350 K are not visible because of negligible diffusion). (b) MSD of the Li^+ ions in the LBH and LCBH systems at 500 K. The inset shows the MSD of B in the LCBH system for the temperature range 250–500 K. The MSD of B was almost zero below the transition temperature (350 K) and saturated at a specific value above the transition temperature.

the MSD saturated at about 7 \AA^2 , indicating reorientational motion of $\text{CB}_{11}\text{H}_{12}^-$ around the respective center of mass. The MSD values were approximately half of the square diameter of a quasispherical large-cage-like anion. Additionally, we confirmed that the centers of mass for both anions did not show translational motion within the examined temperature range, confirming the structural stability. The above results showed full rotation of the anions around the center of mass above the transition temperature. A detailed study of the anion reorientational motion is given in Section 3.4. The above behavior confirmed that despite the high anion reorientational motion, the anions were translationally immobile at their respective equilibrium positions in both the LBH and LCBH systems.

The diffusion coefficients of the Li^+ ions were calculated from the diffusive regions of the MSD for both systems, and the conductivity was calculated using eq 5. The conductivity of the Li^+ ions plotted against the inverse of the temperature is shown in Figure 4, and it is compared with reported experimental results.³⁹ Both the experimental and calculated results showed similar behavior, and a transition in the slope associated with different activation energies to ensure two different phases was identified for both systems, as already reflected in Figure 2. The activation energy of the LBH system was $E_a = 0.35 \text{ eV}$, which is in excellent agreement with the experimental activation energy (0.34 eV).⁶³ Whereas, the activation energy of the LCBH system was $E_a = 0.22 \text{ eV}$, and the experimental value is 0.24 eV .⁴⁴ The transition temperatures were also different: 475 K for the LBH system (experimental value 590 K)³⁸ and 350 K for the LCBH system (experimental value 390 K).⁴²

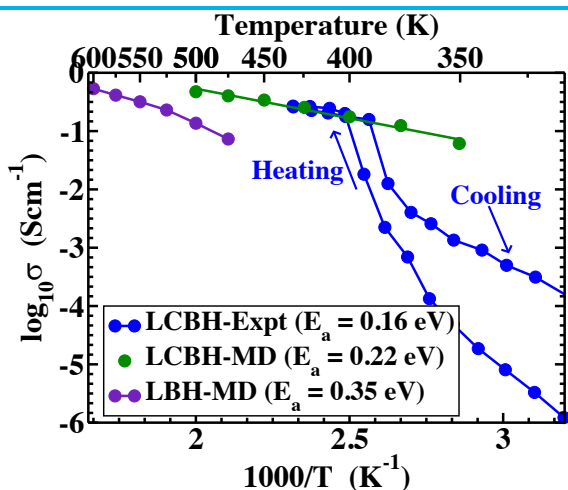


Figure 4. Arrhenius plot of the Li^+ conductivity in the LBH and LCBH systems from MD and experiments (Expt). The results of a previous experimental study²⁹ are also shown for comparison. The calculated conductivity in the low conductivity (below 475 K for LBH and below 350 K) phase was practically zero, which is not shown.

3.3. Microscopic Behavior. The phase transitions in both systems were accompanied by cation and anion redistribution, which is shown by the three-dimensional atomic probability densities in the LT and HT phases. The three-dimensional atomic probability density was generated by merging all of the coordinates into a unit cell. The entire unit cell was then divided into small voxels, and the ions were counted in each voxel. The count in each voxel was normalized by the total count, such that $\int \rho d\Omega = 1$, to generate the atomic probability density profile ρ . The calculated densities were replicated in a $2 \times 2 \times 2$ supercell for better visualization. We calculated the isosurface densities for both the LT and HT phases. The isosurface densities were highly localized for both Li and H in the LT phase, and there was no connectivity among the densities, indicating no diffusion. In contrast, the HT phases (500 K) of both systems showed spread and well-connected densities for Li. The H-density distribution at HT in the LBH system was nearly spherical, whereas it was slightly deformed from the spherical shape in the LCBH system because of C substitution (Figure 5). For the H-density isosurface, each high density was connected by another four neighboring high densities, indicating a four-fold symmetric distribution, which has also been recently reported in a FPMD study.⁴² We also examined the B and C isosurface distributions, which were nearly the same because B and C are connected by strong B–C covalent bonds. There was a slight difference because of the different valences, bond lengths, and bond strengths. However, the Li^+ ion distributions around the C and B atoms were significantly different because of different Coulomb interactions, as shown in Figure 6. The local Li^+ ion distribution around the anions is best visualized by the spatial density distribution (SDD, Figure 6(a)). This was produced by transforming the Li^+ ion coordinates to a selected choice of body fixed axes of the anion. These transformed coordinates were then mapped onto a fine three-dimensional grid and averaged over the length of the simulation using the software package TRAVIS.⁶⁴ From the results, introducing C had a substantial influence on the cation motion and distribution.

In Figure 5 (c,d), a cubic Li^+ ion distribution formed inside the six-coordinated anions, indicating octahedral (Oc) sites. A tetragonal Li^+ ion distribution formed inside the four-coordinated anions, indicating tetrahedral (Tt) sites, as previously reported.⁴⁵ However, the occupancies of the Li^+ ions at the different Li sites (Oc and Tt at HT) were different for the LBH and LCBH systems, as shown in Figure 5 (c,d). For LCBH, there were eight low occupancy Tt sites and four high occupancy Oc sites in each unit cell, and the densities were well connected. The occupancies of the different sites were calculated.⁶⁵ The occupancies of the Oc and Tt sites were 0.96 and 0.04 , respectively. The Oc sites are more energetically favorable for Li^+ ions than the Tt sites because the Li^+ ion faces larger attraction at the Oc sites because of six-coordinated anions. There are four Li^+ ions in each unit cell, so the

Li^+ ion preferably occupies the Oc sites, and the expected hopping mechanism is Oc–Tt–Oc. In contrast, for the LBH system, despite there being energetically preferable Oc sites, the Li^+ ions are forced to occupy the Tt sites, which are not energetically favorable,

to avoid Li–Li repulsion because of the larger number of Li^+ ions in the unit cell, as shown in Figure 5(c). The free energy barriers for both systems were also calculated for both Li- and H- isosurface density calculations using the equation given in Table

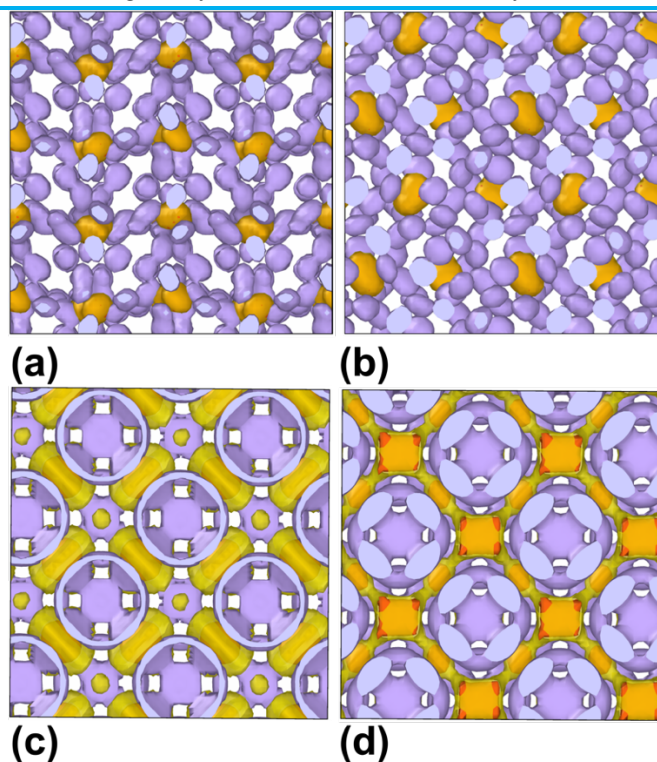


Figure 5. Isosurface density plots of the Li^+ ion with isovalues of $8 \times 10^{-5} \text{ \AA}^{-3}$ (yellow) and $10 \times 10^{-5} \text{ \AA}^{-3}$ (orange), and H with an isovalue of $5 \times 10^{-5} \text{ \AA}^{-3}$ (violet) in a $2 \times 2 \times 2$ supercell obtained with OVITO software.⁶⁶ (a) Low conductivity phase of the LBH system. (b) Low conductivity phase of the LCBH system. (c) High conductivity phase of the LBH system (high density at tetrahedral void and low density at octahedral void formed by anions). (d) High conductivity phase of the LCBH system (moderate density at tetrahedral void and high density at octahedral void formed by anions).

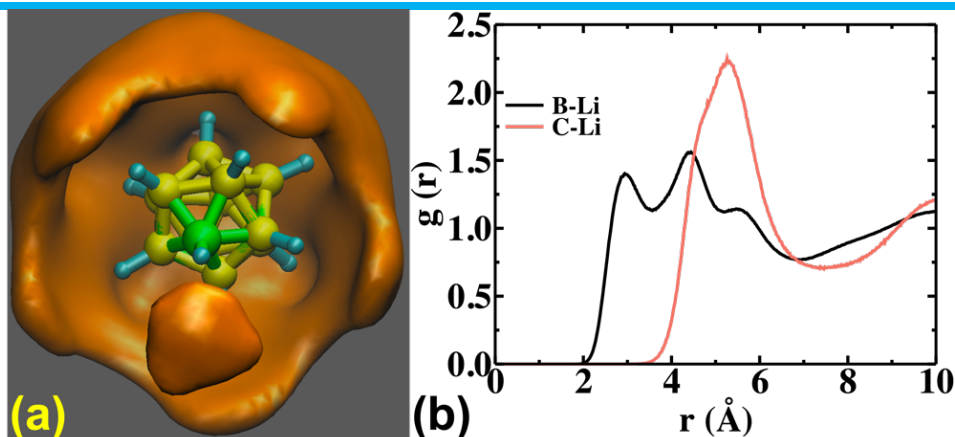


Figure 6. (a) Spatial density distribution (SDD) of Li^+ ions (orange) around $\text{CB}_{11}\text{H}_{12}^-$ (represented by the ball and stick model: B (yellow), H (cyan), and C (green)) at 500 K. The Li^+ ion density around the C is different because of high C–Li repulsion. (b) RDFs ($g(r)$) of B–Li and C–Li pairs for the LCBH system calculated from NPT-MD at 500 K. The different distributions of Li^+ ion around B and C is also reflected.

3. The free energy barrier of Li^+ ion hopping was about 0.43 eV for the LBH system, whereas it was 0.035 eV for the LCBH

resulting in a lower hopping free energy barrier. The reorientational motion was reflected in the MSD of the

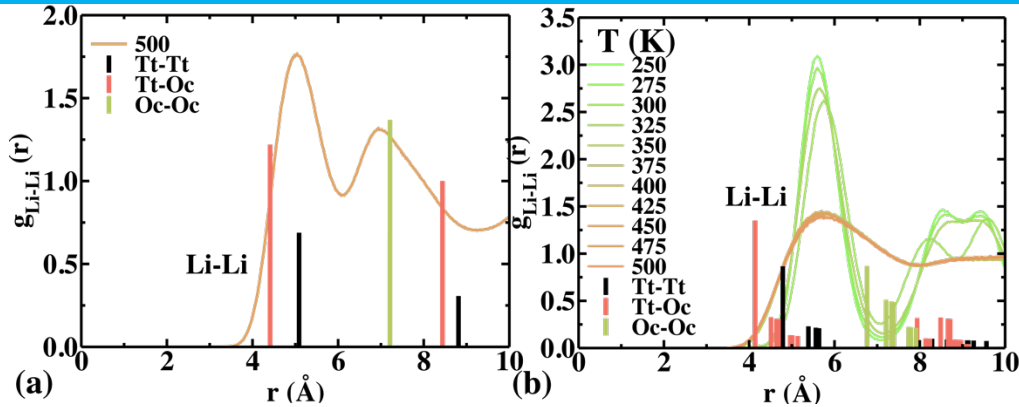


Figure 7. RDF ($g_{\text{Li-Li}}(r)$) of the Li-Li pair at 500 K calculated from NPT-MD for the (a) LBH system and (b) LCBH system. The RDFs among the tetrahedral and octahedral sites are also shown as bar plots (the bar heights are reduced for visualization). The $g(r)$ for LCBH-system shows more liquid like nature than LBH-system.

system. The very large difference might be because of Li-Li correlation in Li^+ ion hopping. However, the free energy barriers of H were low for both systems and their values were also similar, indicating high and similar reorientational rates.

To investigate the hopping route, we also calculated the Li-Li radial distributions function, $g_{\text{Li-Li}}(r)$, for both systems, as shown in Figure 7. The $g_{\text{Li-Li}}(r)$ in LCBH system shows more liquid like nature at high conducting phase than the LBH-system because of high Li^+ ion diffusion among the disordered Li-sites. The first peak perfectly matched the neighboring tetrahedral to tetrahedral site distances for the LBH system, whereas the peak matching in the LCBH system was not as good because of the excellent connectivity among the sites. Thus, the hopping route was either Oc-Tt-Oc or Tt-Oc-Tt, because no other routes existed. In contrast, the high-density Tt-Tt site connectivity is poor for the LBH system because of strong Li^+-Li^+ correlation (see Section 3.5), resulting in longer waiting time and lower diffusion. Therefore, the hopping route in the LBH system must be Tt-Oc-Tt.

Table 3. Free Energy barrier (ΔF) calculated from iso-surface density.

System	ρ_{th} (\AA^{-3})	ρ_{max} (\AA^{-3})	$\Delta F = -k_B T \ln(\frac{\rho_{th}}{\rho_{max}})$ (eV)
Li LBH	6.0×10^{-6}	1.3×10^{-3}	0.430
LCBH	8.8×10^{-5}	2.0×10^{-4}	0.035
H LBH	10.0×10^{-5}	14.0×10^{-5}	0.014
LCBH	7.0×10^{-5}	11.0×10^{-5}	0.019

ρ_{th} = threshold density; ρ_{max} = maximum density

3.4. Influence of Anion Reorientation on Cation Diffusion.

Anion reorientation is a distinct feature in this series of materials, and it deforms the potential landscape of Li^+ ion diffusion,

constituting atoms in the anion. The angular autocorrelation function $\zeta(t')$ can be directly measured by calculating the angular autocorrelation of anions around the center of mass (Figure 7(a)):

$$\zeta(t') = \langle \hat{r}(t) \cdot \hat{r}(t+t') \rangle \quad (6)$$

where \hat{r} is a unit vector connecting the center of mass and B within an anion at time t and $\hat{r}(t+t')$ is the same unit vector after time t' . $\zeta(t')$ as a function of t' for the LCBH system for temperature of 250–500 K is shown in Figure 8. The function does not show any decay in the LT phase. However, after the transition temperature, it decays to zero within a few tens of picoseconds.

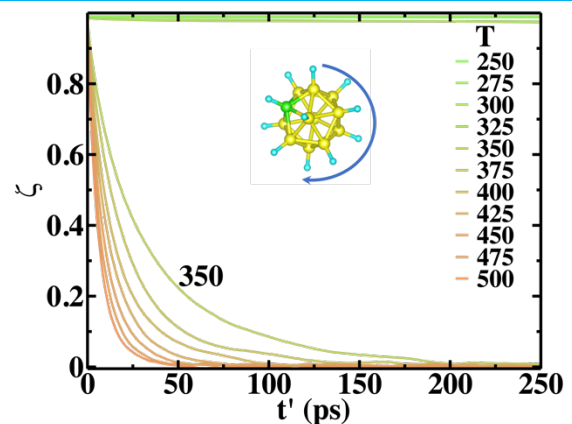


Figure 8. Angular autocorrelation function of the $(\text{CB}_{11}\text{H}_{12})^-$ anion ($\zeta(t')$) as a function of time (t') from NPT-MD simulations at 250–500 K with an interval of 25 K. The function decays as $\sim e^{-\lambda t'}$ within a short time above the order-disorder transition temperature (350 K).

$\zeta(t')$ decays as $e^{-\lambda t'}$, where λ is the decay rate, within a short time. In the LT phase, in the absence of reorientational motion, the structure is ordered. Thus, almost no disordered sites exist for the anions, as well as the Li^+ ions, and the sites are fully occupied, resulting in almost no cation diffusion. Therefore, the MSD and

angular autocorrelation function indicate that in the LT phases for both systems, the anions are rotationally and translationally immobile, whereas the anions are rotationally mobile and translationally immobile in the high conducting phase.

In the LBH system, an anion is coordinated to six Li^+ ions, whereas it is only coordinated to three Li^+ ions in the LCBH system. Thus, the anion reorientational motion of each anion in the LBH system drives two times more cations than in the LCBH system. The Li^+ ions left their local on-sites in LBH system within

diffusion for both the LBH and LCBH systems. We found that the Li^+ ion behavior was almost unchanged after 5 ps. This means that the Li^+ ion disappeared from the nearest H within approximately 5 ps for both the LBH and LCBH systems because of fast anion reorientational motion. It is worth mentioning that the similar times suggest that the reorientational rates of the anions were the same, which was determined by directly comparing the angular autocorrelation functions for both systems (Figure 10). The decay rates were almost the same in spite of C incorporation. In contrast,

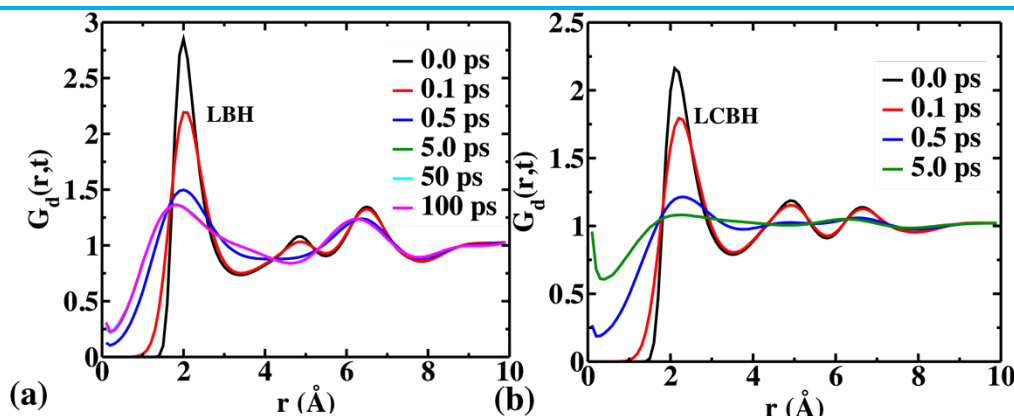


Figure 9. Distinct van Hove correlation function, $G_d(r, t)$, of H-Li for the (a) LBH system and (b) LCBH system at 500 K. The 5 and 50 ps lines are not visible in (a) because they are masked by the 100 ps line.

about 10 ps because of anion reorientation. They quickly jumped from their local on-sites. However, compared with the LCBH system, a larger fraction of Li^+ ions is expected to be unsuccessful

Li^+ ion diffusion in the LCBH system was significantly higher than that in the LBH system. Hence, apart from anion reorientational motion, other influencing factors must play crucial roles in Li^+ ion diffusion, which are discussed in Section 3.5 using the self-part of the van Hove correlation function and logarithmic plots of the MSD.

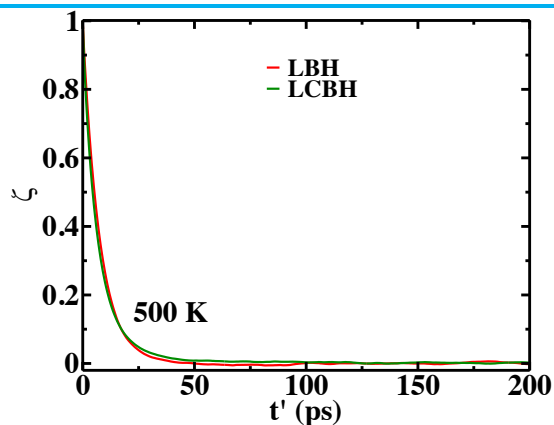


Figure 10. Comparison of anion reorientational motion of $(\text{CB}_{11}\text{H}_{12})^-$ and $(\text{BH})_{12}^{2-}$ at 500 K.

in occupying the next neighboring sites and wait in between the two sites, because there are a smaller number of vacant sites in the LBH system. As a result, despite the quick transition from its local on-sites in LBH system, it does not show long-range diffusion. Local caging is observed in the system, as discussed in the section 3.5.

We calculated the distinct part of the van Hove correlation function for the Li-H pair (Figure 9), which showed very interesting results related to anion reorientation and cation

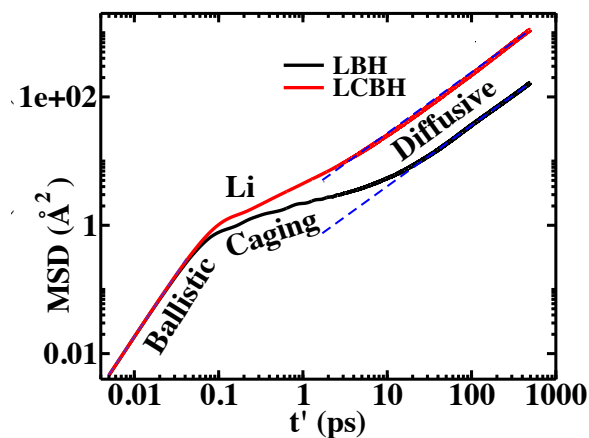


Figure 11. Logarithmic MSD of the Li^+ ions as a function of time (t') for the LBH and LCBH systems at 500 K. The LBH system shows a longer caging effect than the LCBH system. The dashed blue lines show the deviation of the MSD from a straight line.

3.5 Cation-Cation Correlation. The correlation between Li^+ ions was investigated in detail by logarithmic plots of the MSD (Figure 11). Three distinct regions (ballistic, caging, and diffusive) were identified. For both systems, the ballistic region was within 100 fs,

which corresponds to on-site vibration of Li^+ ions. In contrast, the caging region was longer (~ 20 ps) for the LBH system than for the LCBH system (1–2 ps). Thus, the Li^+ ions in the LBH system rapidly left the local on-sites and then waited for a longer time (~ 20 ps) in between two tetrahedral sites, because the neighboring sites were already occupied by other Li^+ ions. Hence, in the LBH system, Li^+ ion hopping was strongly correlated with the motion of other Li^+ ions because of the unavailability of vacant sites. Notably, the longer waiting time for the LBH system was indirectly responsible for increasing the activation energy, resulting in lower diffusion. The Li^+-Li^+ ion correlation can be diminished by introducing Li-site vacancies, as experimentally verified by Kim et al.,³³ who found that Li-ion vacancies enhanced the Li^+ ion conductivity by three orders of magnitude. Conversely, the waiting time for the LCBH system was shorter because there were ample vacant Li sites. Thus, the Li^+ ions did not need to wait long between two sites because the neighboring sites were already empty, which significantly enhanced diffusion.

To understand the Li–Li correlation, we also calculated the self-part of the van Hove correlation function $G_s(r, t')$, as shown in Figure 12 for the Li^+ ions of the HT phases of both systems. A few local maxima can be identified with increasing time (t'). For the LBH system, the first peak near 1 Å corresponds to local on-site vibrations of the Li^+ ions, and the peak broadening is because of the temperature. The second peak indicates Li^+ ion hopping from the local on-sites to the neighboring sites. This occurred within 10–20 ps, which is consistent with the calculated Li–Li RDFs (the second peak in Figure 12(a) is close to the first peak distance in Figure 7(a)). For the LBH system (Figure 12(a)), there was a long waiting time (unless a second peak formed, which was after approximately 10 ps), whereas hopping occurred within a short time (less than 5 ps) in the LCBH system. The peaks in Figure 12(a) are sharper than those in Figure 12(b), because the sites are well connected in the LCBH system.

Table 4. Volume per formula unit and Transition temperature for different system in this series.

System	Volume (f.u.) (\AA^3)	Transition Temperature (K)
$\text{Li}_2\text{B}_{12}\text{H}_{12}$	219.60	590 ³⁸
$\text{Na}_2\text{B}_{12}\text{H}_{12}$	261.63	529 ⁶⁷
$\text{K}_2\text{B}_{12}\text{H}_{12}$	300.87	--
$\text{LiCB}_{11}\text{H}_{12}$	223.07	390 ⁴²
$\text{NaCB}_{11}\text{H}_{12}$	237.57	380 ⁴²
$\text{KCB}_{11}\text{H}_{12}$	238.04	360 ⁴²

3.6. Activation of Anion Reorientation and Entropy-Driven Order–Disorder Phase Transition. A comparison of the reported transition temperatures and corresponding volumes per formula unit is given in Table 4. There is a nice trend between the cell volume and transition temperature. Basically, the cell volume increases to accommodate larger cations, which reduces the transition temperature. For larger cell volume, there are a few important factors that are responsible for lowering the transition temperature, such as (a) anions find larger interstitial space, which eases the anion reorientational motion and (b) the cation number density decreases, which decreases the anion–cation interaction and provides the anions with greater freedom to reorient. In fact, $(1-x)\text{Li}(\text{CB}_9\text{H}_{10})-x\text{Li}(\text{CB}_{11}\text{H}_{12})$ solid solution shows a systematic increase in volume with increasing x and decreasing transition temperature.³⁴ At around $x = 0.3$, the composition has the highest volume with the lowest transition temperature. Other factors, such as a monovalent anion, also decrease the anion–cation and anion–anion interactions. The anion shape and size also play important roles in decreasing the transition temperature.

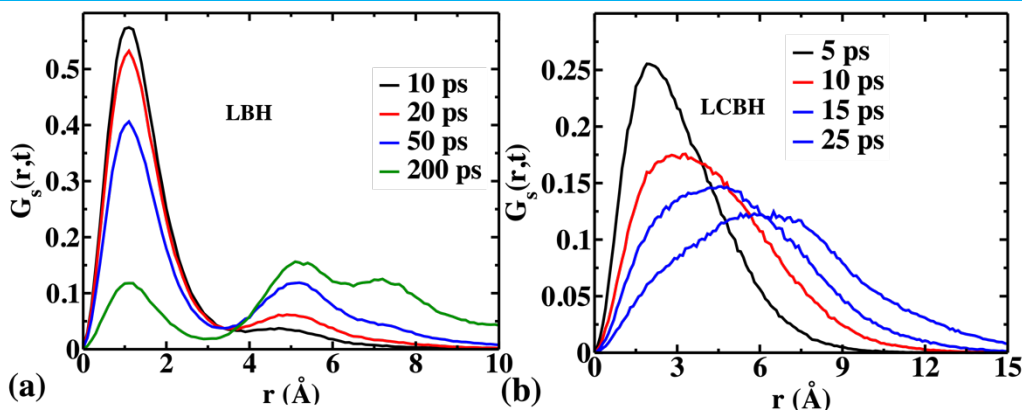


Figure 12. Self-van Hove correlation function of Li^+ ($G_s(r, t)$) for the (a) LBH system and (b) LCBH system at 500 K. The peaks for the LBH system are sharp, whereas the peaks for the LCBH system are relatively wide.

4. CONCLUSION

Force-field-based MD simulations showed the order–disorder phase transition associated with high anion reorientational motion and change in the volume. Additionally, we performed comparative analysis of the microscopic route of cation transport inside the face-centered anions. The structural insight at HT will provide a better understanding of the LCBH system, because it is not accessible by experiments. Surprisingly, both systems exhibited practically the same anion reorientational rates in spite of the different valance anions. However, cation diffusion was relatively large for the LCBH system compared with the LBH system, which is because the vacant Li sites reduce cation–cation correlation in Li^+ ion diffusion. Finally, we determined the factors responsible for lowering the order–disorder transition temperature, which has far-reaching significance beyond the materials in this series.

■ ASSOCIATED CONTENT

*Supporting Information

■ AUTHOR INFORMATION

Corresponding Author

*E-mail: kartik.sau@gmail.com.

ORCID

0000–0003–2432–2015

Notes

The authors declare no competing financial interest.

ACKNOWLEDGMENT

We thank Tim Cooper, PhD, from Edanz Group (<https://en-author-services.edanzgroup.com/ac>) for editing a draft of this manuscript. We gratefully acknowledge the Center for Computational Materials Science of Institute for Materials Research, Tohoku University for the use of MASAMUNE-IMR (MAterial science Supercomputing system for Advanced MUltiscale simulations towards NEXt-generation-Institute for Materials Research) (Project No -19S0010).

■ REFERENCES

- (1) Goodenough, J. B.; Hong, H. Y. P.; Kafalas, J. A. Fast Na⁺-Ion Transport in Skeleton Structures. *Mater. Res. Bull.* **1976**, *11* (2), 203–220.
- (2) Von Alpen, U.; Bell, M. F.; Höfer, H. H. Compositional Dependence of the Electrochemical and Structural Parameters in the Nasicon System ($\text{Na}_{1+x}\text{SixZr}_2\text{P}_3\text{-XO}_{12}$). *Solid State Ionics* **1981**, *3–4* (C), 215–218.
- (3) Hooper, A. A Study of the Electrical Properties of Single-Crystal and Polycrystalline β -Alumina Using Complex Plane Analysis. *J. Phys. D. Appl. Phys.* **1977**, *10* (11), 1487–1496.
- (4) Udovic, T. J.; Matsuo, M.; Unemoto, A.; Verdal, N.; Stavila, V.; Skripov, A. V.; Rush, J. J.; Takamura, H.; Orimo, S. Sodium Superionic Conduction in $\text{Na}_2\text{B}_{12}\text{H}_{12}$. *Chem. Commun.* **2014**, *50* (28), 3750–3752.
- (5) Fergus, J. W. Ion Transport in Sodium Ion Conducting Solid Electrolytes. *Solid State Ionics* **2012**, *227*, 102–112.
- (6) Famprikis, T.; Canepa, P.; Dawson, J. A.; Islam, M. S.; Masquelier, C. Fundamentals of Inorganic Solid-State Electrolytes for Batteries. *Nat. Mater.* **2019**, *18* (12), 1278–1291.
- (7) Bron, P.; Johansson, S.; Zick, K.; Der G nne, J. S. A.; Dehnen, S.; Roling, B. $\text{Li}_{10}\text{SnP}_2\text{S}_{12}$: An Affordable Lithium Superionic Conductor. *J. Am. Chem. Soc.* **2013**, *135* (42), 15694–15697.
- (8) Kamaya, N.; Homma, K.; Yamakawa, Y.; Hirayama, M.; Kanno, R.; Yonemura, M.; Kamiyama, T.; Kato, Y.; Hama, S.; Kawamoto, K.; et al. A Lithium Superionic Conductor. *Nat. Mater.* **2011**, *10* (9), 682–686.
- (9) Takada, K. Progress and Prospective of Solid-State Lithium Batteries. *Acta Mater.* **2013**, *61* (3), 759–770.
- (10) Sahu, G.; Lin, Z.; Li, J.; Liu, Z.; Dudney, N.; Liang, C. Air-Stable, High-Conduction Solid Electrolytes of Arsenic-Substituted Li_4SnS_4 . *Energy Environ. Sci.* **2014**, *7* (3), 1053–1058.
- (11) Thangadurai, V.; Narayanan, S.; Pinzaru, D. Garnet-Type Solid-State Fast Li Ion Conductors for Li Batteries: Critical Review. *Chem. Soc. Rev.* **2014**, *43* (13), 4714–4727.
- (12) Sau, K.; Ikeshoji, T.; Kim, S.; Takagi, S.; Akagi, K.; Orimo, S. Reorientational Motion and Li⁺-Ion Transport in $\text{Li}_2\text{B}_{12}\text{H}_{12}$ System: Molecular Dynamics Study. *Phys. Rev. Mater.* **2019**, *3* (7), 075402.
- (13) Latroche, M.; Blanchard, D.; Cuevas, F.; El Kharbachi, A.; Hauback, B. C.; Jensen, T. R.; de Jongh, P. E.; Kim, S.; Nazer, N. S.; Ngene, P.; et al. Full-Cell Hydride-Based Solid-State Li Batteries for Energy Storage. *Int. J. Hydrogen Energy* **2019**, *44* (15), 7875–7887.
- (14) Mohtadi, R.; Orimo, S. The Renaissance of Hydrides

- as Energy Materials. *Nat. Rev. Mater.* **2016**, *2* (3), 1–16.
- (15) Sau, K.; Ikeshoji, T.; Roy, S. Role of Divalent Cation (Ba) Substitution in Li⁺ Ion Conductor LiTi₂(PO₄)₃: Molecular Dynamics Study. *Phys. Chem. Chem. Phys.* **2020**, *2*.
- (16) Pramanik, K.; Sau, K.; Kumar, P. P. Role of Framework Flexibility in Ion Transport: A Molecular Dynamics Study of LiM₂IV(PO₄)₃. *J. Phys. Chem. C* **2020**, *124* (7), 4001–4009.
- (17) Boulineau, S.; Courty, M.; Tarascon, J. M.; Viallet, V. Mechanochemical Synthesis of Li-Argyrodite Li₆PS₅X (X = Cl, Br, I) as Sulfur-Based Solid Electrolytes for All Solid State Batteries Application. *Solid State Ionics* **2012**, *221*, 1–5.
- (18) Rao, R. P.; Adams, S. Studies of Lithium Argyrodite Solid Electrolytes for All-Solid-State Batteries. *Phys. Status Solidi Appl. Mater. Sci.* **2011**, *208* (8), 1804–1807.
- (19) Maekawa, H.; Matsuo, M.; Takamura, H.; Ando, M.; Noda, Y.; Karahashi, T.; Orimo, S. Halide-Stabilized LiBH₄, a Room-Temperature Lithium Fast-Ion Conductor. *J. Am. Chem. Soc.* **2009**, *131* (3), 894–895.
- (20) Unemoto, A.; Yoshida, K.; Ikeshoji, T.; Orimo, S. Bulk-Type All-Solid-State Lithium Batteries Using Complex Hydrides Containing Cluster-Anions. *Mater. Trans.* **2016**, *57* (9), 1639–1644.
- (21) Bernuy-Lopez, C.; Manalastas, W.; Lopez Del Amo, J. M.; Aguadero, A.; Aguesse, F.; Kilner, J. A. Atmosphere Controlled Processing of Ga-Substituted Garnets for High Li-Ion Conductivity Ceramics. *Chem. Mater.* **2014**, *26* (12), 3610–3617.
- (22) Thangadurai, V.; Weppner, W. Li₆Ala₂Ta₂O₁₂ (A = Sr, Ba): Novel Garnet-like Oxides for Fast Lithium Ion Conduction. *Adv. Funct. Mater.* **2005**, *15* (1), 107–112.
- (23) Arbi, K.; Hoelzel, M.; Kuhn, a; Garc, F.; Sanz, J. Structural Factors That Enhance Lithium Mobility in Fast-Ion Li⁺. *Inorg. Chem.* **2013**, *52* (Figure 1), 9290–9296.
- (24) Inaguma, Y. HIGH IONIC CONDUCTIVITY IN LITHIUM LANTHANUM TITANATE Yoshiyuki. *Solid State Commun.* **1993**, *86* (10), 689–693.
- (25) Thangadurai, V.; Shukla, A. K.; Gopalakrishnan, J. Li_{0.65} Sr_{0.35} B_{1.3} B'_{1.7} O₉ (B = Ti, Zr; B' = Nb, Ta): New Lithium Ion Conductors Based on the Perovskite Structure †. *Chem. Mater.* **1999**, *11* (3), 835–839.
- (26) Unemoto, A.; Matsuo, M.; Orimo, S. I. Complex Hydrides for Electrochemical Energy Storage. *Adv. Funct. Mater.* **2014**, *24* (16), 2267–2279.
- (27) Tang, W. S.; Matsuo, M.; Wu, H.; Stavila, V.; Zhou, W.; Talin, A. A.; Soloninin, A. V.; Skoryunov, R. V.; Babanova, O. A.; Skripov, A. V.; et al. Liquid-Like Ionic Conduction in Solid Lithium and Sodium Monocarba-Closo-Decaborates Near or at Room Temperature. *Adv. Energy Mater.* **2016**, *6* (8), 1502237.
- (28) Tang, W. S.; Matsuo, M.; Wu, H.; Stavila, V.; Unemoto, A.; Orimo, S. I.; Udovic, T. J. Stabilizing Lithium and Sodium Fast-Ion Conduction in Solid Polyhedral-Borate Salts at Device-Relevant Temperatures. *Energy Storage Mater.* **2016**, *4*, 79–83.
- (29) Tang, W. S.; Unemoto, A.; Zhou, W.; Stavila, V.; Matsuo, M.; Wu, H.; Orimo, S.; Udovic, T. J. Unparalleled Lithium and Sodium Superionic Conduction in Solid Electrolytes with Large Monovalent Cage-like Anions. *Energy Environ. Sci.* **2015**, *8* (12), 3637–3645.
- (30) Kweon, K. E.; Varley, J. B.; Shea, P.; Adelstein, N.; Mehta, P.; Heo, T. W.; Udovic, T. J.; Stavila, V.; Wood, B. C. Structural, Chemical, and Dynamical Frustration: Origins of Superionic Conductivity in Closo -Borate Solid Electrolytes. *Chem. Mater.* **2017**, *29* (21), 9142–9153.
- (31) Sau, K.; Ikeshoji, T.; Kim, S.; Takagi, S.; Akagi, K. Molecular Dynamics Study of Fast Li⁺ Ion Transport in Closo- Boranes . **2019**, *15* (2016), 17748.
- (32) Kim, S.; Oguchi, H.; Toyama, N.; Sato, T.; Takagi, S.; Otomo, T.; Arunkumar, D.; Kuwata, N.; Kawamura, J.; Orimo, S. A Complex Hydride Lithium Superionic Conductor for High-Energy-Density All-Solid-State Lithium Metal Batteries. *Nat. Commun.* **2019**, *10* (1), 1081.
- (33) Kim, S.; Toyama, N.; Oguchi, H.; Sato, T.; Takagi, S.; Ikeshoji, T.; Orimo, S. I. Fast Lithium-Ion Conduction in Atom-Deficient Closo-Type Complex Hydride Solid Electrolytes. *Chem. Mater.* **2018**, *30* (2), 386–391.
- (34) Kim, S.; Kisu, K.; Takagi, S.; Oguchi, H.; Orimo, S. I. Complex Hydride Solid Electrolytes of the Li(CB₉H₁₀)-Li(CB₁₁H₁₂) Quasi-Binary System: Relationship between the Solid Solution and Phase Transition, and the Electrochemical Properties. *ACS Appl. Energy Mater.* **2020**, *3* (5), 4831–4839.
- (35) Lundén, A. Evidence for and against the Paddle-Wheel Mechanism of Ion Transport in Superionic Sulphate Phases. *Solid State Commun.* **1988**, *65* (10), 1237–1240.
- (36) Jansen, M. Volume Effect or Paddle-Wheel Mechanism—Fast Alkali-Metal Ionic Conduction in

- Solids with Rotationally Disordered Complex Anions. *Angew. Chemie Int. Ed. English* **1991**, *30* (12), 1547–1558.
- (37) Wilmer, D.; Funke, K.; Witschas, M.; Banhatti, R. D.; Jansen, M.; Korus, G.; Fitter, J.; Lechner, R. E. Anion Reorientation in an Ion Conducting Plastic Crystal - Coherent Quasielastic Neutron Scattering from Sodium Ortho-Phosphate. *Phys. B Condens. Matter* **1999**, *266* (1–2), 60–68.
- (38) Sau, K.; Ikeshoji, T. Origin of Fast Ion Conduction in Na₃PS₄: Insight from Molecular Dynamics Study. *J. Phys. Chem. C* **2020**, acs.jpcc.0c04476.
- (39) Famprikis, T.; Dawson, J. A.; Fauth, F.; Clemens, O.; Suard, E.; Fleutot, B.; Courty, M.; Chotard, J.-N.; Islam, M. S.; Masquelier, C. A New Superionic Plastic Polymorph of the Na⁺ Conductor Na₃PS₄. *ACS Mater. Lett.* **2019**, *1* (6), 641–646.
- (40) Dawson, J. A.; Canepa, P.; Clarke, M. J.; Famprikis, T.; Ghosh, D.; Islam, M. S. Toward Understanding the Different Influences of Grain Boundaries on Ion Transport in Sulfide and Oxide Solid Electrolytes. *Chem. Mater.* **2019**, *31* (14), 5296–5304.
- (41) Zhang, Z.; Roy, P. N.; Li, H.; Avdeev, M.; Nazar, L. F. Coupled Cation-Anion Dynamics Enhances Cation Mobility in Room-Temperature Superionic Solid-State Electrolytes. *J. Am. Chem. Soc.* **2019**, *141* (49), 19360–19372.
- (42) Dimitrievska, M.; Wu, H.; Stavila, V.; Babanova, O. A.; Skoryunov, R. V.; Soloninin, A. V.; Zhou, W.; Trump, B. A.; Andersson, M. S.; Skripov, A. V.; et al. Structural and Dynamical Properties of Potassium Dodecahydro-Monocarpa-Closo-Dodecaborate: KCB₁₁H₁₂. *J. Phys. Chem. C* **2020**.
- (43) Verdal, N.; Her, J. H.; Stavila, V.; Soloninin, A. V.; Babanova, O. A.; Skripov, A. V.; Udovic, T. J.; Rush, J. J. Complex High-Temperature Phase Transitions in Li₂B₁₂H₁₂ and Na₂B₁₂H₁₂. *J. Solid State Chem.* **2014**, *212*, 81–91.
- (44) Tang, W. S.; Unemoto, A.; Zhou, W.; Stavila, V.; Matsuo, M.; Wu, H.; Orimo, S.; Udovic, T. J. Unparalleled Lithium and Sodium Superionic Conduction in Solid Electrolytes with Large Monovalent Cage-like Anions. *Energy Environ. Sci.* **2015**, *8* (12), 3637–3645.
- (45) Kweon, K. E.; Varley, J. B.; Shea, P.; Adelstein, N.; Mehta, P.; Heo, T. W.; Udovic, T. J.; Stavila, V.; Wood, B. C.; Shea, P.; et al. Structural, Chemical, and Dynamical Frustration: Origins of Superionic Conductivity in Closo-Borate Solid Electrolytes. *Chem. Mater.* **2017**, *29* (21), 9142–9153.
- (46) Varley, J. B.; Kweon, K.; Mehta, P.; Shea, P.; Heo, T. W.; Udovic, T. J.; Stavila, V.; Wood, B. C. Understanding Ionic Conductivity Trends in Polyborane Solid Electrolytes from Ab Initio Molecular Dynamics. *ACS Energy Lett.* **2017**, *2* (1), 250–255.
- (47) Dimitrievska, M.; Shea, P.; Kweon, K. E.; Bercx, M.; Varley, J. B.; Tang, W. S.; Skripov, A. V.; Stavila, V.; Udovic, T. J.; Wood, B. C. Carbon Incorporation and Anion Dynamics as Synergistic Drivers for Ultrafast Diffusion in Superionic LiCB₁₁H₁₂ and NaCB₁₁H₁₂. *Adv. Energy Mater.* **2018**, *8* (15).
- (48) Takagi, S.; Ikeshoji, T.; Sato, T.; Orimo, S. Pseudorotating Hydride Complexes with High Hydrogen Coordination: A Class of Rotatable Polyanions in Solid Matter. *Appl. Phys. Lett.* **2020**, *116* (17), 173901.
- (49) Deng, Y.; Eames, C.; Chotard, J.-N.; Lalère, F.; Seznec, V.; Emge, S.; Pecher, O.; Grey, C. P.; Masquelier, C.; Islam, M. S. Structural and Mechanistic Insights into Fast Lithium-Ion Conduction in Li₄SiO₄-Li₃PO₄ Solid Electrolytes. *J. Am. Chem. Soc.* **2015**, *137* (28), 9136–9145.
- (50) Padma Kumar, P.; Yashonath, S. Structure, Conductivity, and Ionic Motion in Na_{1+x}Zr₂Si_xP_{3-x}O₁₂: A Simulation Study. *J. Phys. Chem. B* **2002**, *106* (28), 7081–7089.
- (51) Plimpton, S. Fast Parallel Algorithms for Short-Range Molecular Dynamics. *J. Comput. Phys.* **1995**, *117* (1), 1–19.
- (52) Hoover, W. G. Constant-Pressure Equations of Motion. *Phys. Rev. A* **1986**, *34* (3), 2499–2500.
- (53) Kresse, G.; Hafner, J. Ab Initio Molecular Dynamics for Liquid Metals. *Phys. Rev. B* **1993**, *47* (1), 558.
- (54) Miedema, A. R. The Electronegativity Parameter for Transition Metals: Heat of Formation and Charge Transfer in Alloys. *J. Less-Common Met.* **1973**, *32* (1), 117–136.
- (55) P.E., B. Projector Augmented-Wave Method. *Phys. Rev. B* **1994**, *50* (24), 17953–17979.
- (56) Kresse, G.; Joubert, D. From Ultrasoft Pseudopotentials to the Projector Augmented-Wave Method. *Phys. Rev. B - Condens. Matter Mater. Phys.* **1999**, *59* (3), 1758–1775.
- (57) M. Dion; Rydberg, H.; Schroder, E.; Langreth, D. C.; B. I. Lundqvist. Van DerWaals Density Functional for General Geometries. *Phys. Rev. Lett.* **2004**, *92* (June), 246401.
- (58) Román-Pérez, G.; Soler, J. M. Efficient Implementation of a van Der Waals Density

- Functional: Application to Double-Wall Carbon Nanotubes. *Phys. Rev. Lett.* **2009**, *103* (9), 1–4.
- (59) Jiří Klimeš; Bowler, D. R.; Michaelides, A. Van Der Waals Density Functionals Applied to Solids. *Phys. Rev. B* **2011**, *83*, 19513.
- (60) Hopkins, P.; Fortini, A.; Archer, A. J.; Schmidt, M. The van Hove Distribution Function for Brownian Hard Spheres: Dynamical Test Particle Theory and Computer Simulations for Bulk Dynamics. *J. Chem. Phys.* **2010**, *133* (22), 1–18.
- (61) Paskevicius, M.; Pitt, M. P.; Brown, D. H.; Sheppard, D. A.; Chumphongphan, S.; Buckley, C. E. First-Order Phase Transition in the $\text{Li}_2\text{B}_{12}\text{H}_{12}$ System. *Phys. Chem. Chem. Phys. Phys. Chem. Chem. Phys.* **2013**, *15*, 15825–15828.
- (62) Sau, K.; Ikeshoji, T.; Takagi, S.; Orimo, S.; Errandonea, D.; Chu, D.; Cazorla, C. Colossal Barocaloric Effects in the Complex Hydride $\text{Li}_2\text{B}_{12}\text{H}_{12}$. **2020**, 1–8.
- (63) Teprovich, J. A.; Colón-Mercado, H.; Washington II, A. L.; Ward, P. A.; Greenway, S.; Missimer, D. M.; Hartman, H.; Velten, J.; Christian, J. H.; Zidan, R. Bi-Functional $\text{Li}_2\text{B}_{12}\text{H}_{12}$ for Energy Storage and Conversion Applications: Solid-State Electrolyte and Luminescent down-Conversion Dye. *J. Mater. Chem. A* **2015**, *3* (45), 22853–22859.
- (64) Brehm, M.; Kirchner, B. TRAVIS - A Free Analyzer and Visualizer for Monte Carlo and Molecular Dynamics Trajectories. *J. Chem. Inf. Model.* **2011**, *51* (8), 2007–2023.
- (65) Tang, W.; Sanville, E.; Henkelman, G. A Grid-Based Bader Analysis Algorithm without Lattice Bias. *J. Phys. Condens. Matter* **2009**, *21* (8).
- (66) Stukowski, A. Visualization and Analysis of Atomistic Simulation Data with OVITO—the Open Visualization Tool. *Model. Simul. Mater. Sci. Eng.* **2010**, *18* (1), 015012.
- (67) Udovic, T. J.; Matsuo, M.; Unemoto, A.; Verdal, N.; Stavila, V.; Skripov, A. V.; Rush, J. J.; Takamura, H.; Orimo, S. Sodium Superionic Conduction in $\text{Na}_2\text{B}_{12}\text{H}_{12}$. *Chem. Commun.* **2014**, *50* (28), 3750–3752.